remote sensing

MDPI

Article

EDH-STNet: An Evaporation Duct Height Spatiotemporal Prediction Model Based on Swin-Unet Integrating Multiple Environmental Information Sources

Hanjie Ji [1,2], Lixin Guo [1], Jinpeng Zhang [2], Yiwen Wei [1,*], Xiangming Guo [2] and Yusheng Zhang [2]

[1] School of Physics, Xidian University, Xi'an 710071, China; jhjxd@stu.xidian.edu.cn (H.J.); lxguo@xidian.edu.cn (L.G.)
[2] National Key Laboratory of Electromagnetic Environment, China Research Institute of Radiowave Propagation, Qingdao 266107, China; zhangjp@crirp.ac.cn (J.Z.); guoxm@crirp.ac.cn (X.G.); zhangys@crirp.ac.cn (Y.Z.)
* Correspondence: ywwei@xidian.edu.cn

Abstract: Given the significant spatial non-uniformity of marine evaporation ducts, accurately predicting the regional distribution of evaporation duct height (EDH) is crucial for ensuring the stable operation of radio systems. While machine-learning-based EDH prediction models have been extensively developed, they fail to provide the EDH distribution over large-scale regions in practical applications. To address this limitation, we have developed a novel spatiotemporal prediction model for EDH that integrates multiple environmental information sources, termed the EDH Spatiotemporal Network (EDH-STNet). This model is based on the Swin-Unet architecture, employing an Encoder–Decoder framework that utilizes consecutive Swin-Transformers. This design effectively captures complex spatial correlations and temporal characteristics. The EDH-STNet model also incorporates nonlinear relationships between various hydrometeorological parameters (HMPs) and EDH. In contrast to existing models, it introduces multiple HMPs to enhance these relationships. By adopting a data-driven approach that integrates these HMPs as prior information, the accuracy and reliability of spatiotemporal predictions are significantly improved. Comprehensive testing and evaluation demonstrate that the EDH-STNet model, which merges an advanced deep learning algorithm with multiple HMPs, yields accurate predictions of EDH for both immediate and future timeframes. This development offers a novel solution to ensure the stable operation of radio systems.

Keywords: evaporation duct height; Swin-Unet; environmental information; hydrometeorological parameters (HMPs); spatiotemporal prediction

Citation: Ji, H.; Guo, L.; Zhang, J.; Wei, Y.; Guo, X.; Zhang, Y. EDH-STNet: An Evaporation Duct Height Spatiotemporal Prediction Model Based on Swin-Unet Integrating Multiple Environmental Information Sources. *Remote Sens.* **2024**, *16*, 4227. https://doi.org/10.3390/rs16224227

Academic Editor: Gad Levy

Received: 2 September 2024
Revised: 20 October 2024
Accepted: 11 November 2024
Published: 13 November 2024

1. Introduction

Evaporation ducts are phenomena resulting from the evaporation of water vapor over extensive water surfaces, such as the sea [1]. A key characteristic of these ducts is the sharp decrease in atmospheric refractivity with increasing height. Evaporation ducts significantly impact the propagation path and energy distribution of radio waves, leading to trapped propagation phenomena. This can result in adverse effects, including detection blind zones, target localization failures, and communication interruptions [2]. Since the evaporation ducts usually exist in the atmosphere below 40 m, they almost cover the communication heights of marine radio systems [3]. Furthermore, the continuous nature of evaporation over the sea contributes to the prevalence of these ducts. Consequently, their wide coverage and frequent occurrence make evaporation ducts a critical atmospheric structure influencing radio wave propagation at sea [4]. The evaporation duct height (EDH) is a key parameter that defines the vertical extent of the duct layer, representing the height between its top and bottom [5]. Given the influence of evaporation ducts on radio wave behavior, accurate detection of EDH is essential to ensure the optimal performance of radio systems operating in marine environments.

The rapid advancement of artificial intelligence has promoted the wide application of machine learning (ML) in the study of evaporation ducts. Early researchers developed purely data-driven prediction models for EDH using fundamental ML methods, leveraging the nonlinear correlations between hydrometeorological parameters (HMPs) and EDH. These ML methods mainly include artificial neural network (ANN) [6,7], multilayer perceptron [8], gradient boosting regression [9], extreme gradient boosting [10], and back propagation network [11]. Compared to traditional evaporation duct diagnostic models, these ML-based models show significantly improved accuracy. Subsequently, researchers undertook comprehensive investigations of measured EDH, identifying its characteristic temporal patterns [12–16]. This prompted the development of EDH prediction models utilizing long short-term memory (LSTM) network, which is particularly effective in processing temporal data [14]. Han et al. [14] successfully developed an EDH prediction model based on LSTM network using data collected from the Yellow Sea of China, achieving superior performance compared to ANN and support vector machine. Zhao et al. [16] not only considered the temporal characteristics of EDH but also applied a data-driven approach to build an LSTM-based prediction model. This model effectively captures internal temporal dynamics of EDH while accurately modeling the relationships between HMPs and EDH. However, due to different meteorological conditions across different marine regions, evaporation ducts usually exhibit regionality and non-uniformity. Existing models typically focus on obtaining EDH at specific fixed locations [6,12–14,17] or along specific navigation routes [8–11,16,18], and thus cannot accurately obtain EDH distribution over larger areas. Therefore, these models cannot comprehensively detect regional evaporation ducts, thereby failing to provide complete protection for marine radio systems.

Previously, researchers have conducted regional prediction studies of evaporation ducts utilizing numerical forecasting models [19,20]. These studies typically incorporate meteorological reanalysis data as initial fields and boundary conditions while employing advanced numerical weather forecasting models, such as the Weather Research and Forecasting model (WRF) [19] and the fifth version of the mesoscale model (MM5) [21]. Compared to developed ML models, numerical forecasting models require high-performance computing resources and extended computation times, which notably limit their practical applications. These numerical models simulate marine and atmospheric physical processes based on fundamental physical equations, performing calculations through the discretization of these equations. Consequently, they rely heavily on accurate initial fields and boundary conditions. In contrast, the developed ML models can automatically learn patterns and relationships of evaporation ducts from large datasets. This capability allows for effective predictions under diverse environmental conditions, showcasing greater practicality and adaptability. According to the recently revised standard of International Telecommunication Union Recommendation (ITU-R) P.453-14 [22], researchers [23] have employed the Kriging spatial interpolation method to process data obtained from observation stations for constructing a digital map of atmospheric refractive index parameters. However, the Kriging interpolation primarily focuses on the estimation of values for unobserved areas based on known or neighboring regional data. A significant limitation of this method is its inadequate consideration of the temporal dependencies inherent within the data. For evaporative ducts, temporal dependencies are crucial as they elucidate the dynamic characteristics that evolve over time. Therefore, relying solely on spatial interpolation is inadequate for achieving a comprehensive understanding of how temporal variations impact evaporation ducts.

In previous studies, convolutional neural networks (CNNs) with U-shaped Encoder–Decoder architecture have excelled in computer vision (CV), particularly in image segmentation (IS) [24]. This architecture effectively extracts spatial correlations and semantic information through the Encoder while achieving precise pixel-level reconstructions via the Decoder. IS fundamentally involves using known grid data to produce new grid data [25], enabling many CV networks to process grid data with temporal characteristics, thereby excelling in spatiotemporal prediction. Han et al. [25] built a convective precipitation

prediction model using the Unet. Spatiotemporal prediction requires models to accurately capture the spatial correlations and temporal variations in grid data to address complex spatiotemporal dynamics. However, CNNs are limited by their receptive fields, which restrict their ability to perceive global features and long-term spatiotemporal characteristics. This limitation arises because convolutional operations are mainly designed for local feature extraction, often ignoring global and long-term correlations. Inspired by the success of the Transformer in natural language processing, scholars have applied it to CV and proposed the *Visual Transformer* [26]. The *shifted window Transformer* (Swin-Transformer) [27] employs a shifted window mechanism to restrict attention to non-overlapping local windows, facilitating information exchange between adjacent windows to incorporate global information comprehensively. It has also been widely applied in spatiotemporal prediction, including weather forecasting [28–30]. Later, Cao et al. [31] proposed Swin-Unet, which is entirely based on the Swin-Transformer. The Swin-Unet utilizes consecutive Swin-Transformer blocks as the Encoder, effectively capturing local and global features. By integrating the Swin-Transformer into the U-shaped Encoder–Decoder architecture, Swin-Unet enhances its capability to interpret semantic features more effectively.

In summary, to address the limitations of existing models in EDH spatiotemporal prediction, a novel hydrometeorological data-driven model, termed the EDH spatiotemporal network (EDH-STNet), has been developed using Swin-Unet. This model leverages the strengths of Swin-Unet to effectively capture the temporal variations in the spatial distribution of EDH, combining the efficient feature extraction capabilities of the Swin-Transformer with the Unet architecture's global modeling abilities. The EDH-STNet further incorporates multiple HMPs as environmental prior information, enhancing its capacity to model the relationships between these parameters and EDH. It not only includes key HMPs such as temperature, wind, and humidity but also incorporates previously overlooked HMPs, allowing for a more comprehensive understanding of the complex interactions between the marine environment and evaporation ducts. This holistic approach leads to more accurate predictions and interpretations of EDH spatiotemporal variations. Performance testing of the EDH-STNet model and comparative analysis with various baseline models demonstrate its superior prediction accuracy. The model effectively captures the intricate spatiotemporal features of EDH, providing a comprehensive view of its variations within the study area.

The rest of this article is organized as follows: Section 2 introduces the data source and how the EDH spatiotemporal distribution is calculated. Section 3 details the methodology employed for developing the EDH-STNet model. The prediction results of the EDH-STNet model and corresponding analysis are detailed in Section 4. Finally, the conclusion is presented in Section 5.

2. Data Source and Calculation

2.1. ERA5 Reanalysis Data

The utilization of publicly available ERA5 reanalysis data from the European Centre for Medium-Range Weather Forecasts (ECMWF) provides a novel approach for obtaining the distribution of evaporation ducts over large sea regions [32]. The ERA5 reanalysis dataset is a comprehensive global meteorological resource developed by ECMWF, which integrates meteorological observations from various sources, including ground-based stations, ships, radiosondes, aircraft, and satellites. As a result, ERA5 offers atmospheric and surface parameters with high temporal and spatial resolution, making it a valuable tool for accurately modeling and analyzing hydrometeorological phenomena, such as evaporation duct characteristics in marine environments.

First, this article extracts HMPs from the ERA5 for calculating EDH, which include atmospheric temperature (AT), atmospheric pressure (AP), u-component of wind, v-component of wind, dewpoint temperature (DT), and sea surface temperature (SST). The extracted HMPs and corresponding reanalysis heights are shown in Table 1.

Table 1. Extracted HMPs and corresponding reanalysis heights.

HMP	Reanalysis Height	Unit
AT	2 m	°C
DT	2 m	°C
u-component of wind	10 m	m/s
v-component of wind	10 m	m/s
AP	Surface	hPa
SST	Surface	°C
EVP	Surface	m of water equivalent
SLHF	Surface	J/m
TP	Surface	m
SWH	Mean height of the highest third of waves	m

Where the *u*- and *v*-components of wind are used to calculate the WS:

$$WS = \sqrt{u^2 + v^2} \tag{1}$$

where u and v are the *u*- and *v*-components of wind, respectively. The RH can be calculated by inputting the AT and DT into the Magnus–Tetens approximation equation [33,34]:

$$RH = \exp\left(\frac{17.625 \times DT}{243.04 + DT} - \frac{17.625 \times T}{243.04 + T}\right) \times 100 \tag{2}$$

Furthermore, previous studies have shown that in addition to the five HMPs used to calculate EDH, other HMPs such as evaporation (EVP), surface latent heat flux (SLHF), total precipitation (TP), and sufficient wave height (SWH) also influence the characteristics of evaporation ducts [35–37]. Fortunately, the neural network model can accept more HMPs as inputs. Therefore, this article extracts these four additional HMPs from the ERA5 dataset and incorporates them into the prediction model as environmental prior information alongside the initial five HMPs. This method enables the prediction model to comprehensively consider the impacts of marine environment on evaporation ducts. In this article, the latitude and longitude resolutions for AT, AP, *u*-component of wind, *v*-component of wind, DT, SST, EVP, SLHF, and TP are uniformly set at 0.25°. In contrast, the latitude and longitude resolution for SWH is 0.5°. To ensure uniformity across all parameters, bilinear interpolation was applied to the SWH data.

2.2. Calculation of Atmospheric Refraction Characteristics

In the lower atmosphere, refraction index n remains relatively constant across the entire radio frequency range, typically ranging between 1.00025 and 1.00040 [38,39]. To describe slight variations in the refractive index, aiding radio wave propagation calculations, the atmospheric refractivity N is introduced:

$$N = (n - 1) \times 10^6 \tag{3}$$

Additionally, the atmospheric refraction is influenced by the variation in the gradient of the propagating medium in the vertical direction. It depends on meteorological parameters such as AT, AP, and water vapor pressure (WVP). To account for the impact of the Earth's curvature on radio wave propagation, a flat Earth model is commonly applied, treating the spherical Earth surface as flat. Accordingly, the atmospheric modified refractivity M can be given by [1]:

$$M(z) = N + \left(\frac{z}{R_e}\right) \times 10^6 \approx N(z) + 0.157z = \frac{77.6}{T} \times \left(P + \frac{4810e}{T}\right) + 0.157z \tag{4}$$

where h is height; R_e is the Earth's radius; and P, T, and e are the AP, AT, and WVP profiles, respectively. The propagation of radio waves is primarily affected by the vertical gradient of the modified refractivity (i.e., dM/dz). When $dM/dz < 0$, the curvature of radio wave rays becomes smaller than the curvature of the Earth. In this case, the radio waves can become trapped within a certain thickness of the atmospheric layer, which is called the atmospheric duct. Among the various types of ducts, evaporation ducts are particularly significant for marine radio systems due to their high frequency and long duration.

2.3. Naval Postgraduate School Evaporation Duct Model

The Naval Postgraduate School (NPS) model [40] is an advanced evaporation duct prediction tool that is currently operationally utilized by the U.S. Navy. This model employs the Coupled Ocean-Atmosphere Response Experiment (COARE) bulk flux algorithm, derived from extensive long-term oceanic surveys, along with empirical relationships based on oceanic experiments, marking a significant advancement over the Paulus–Jeske model [41]. Subsequently, Babin et al. [40] conducted a comparative analysis of the NPS model alongside the Naval Warfare Assessment model, the Naval Research Laboratory model, and the Babin–Young–Carton (BYC) model [42]. By evaluating the predicted evaporation duct profiles against measured profiles, they provided insightful analytical results. Their findings indicated that both the NPS and BYC models are the most effective for estimating the EDH and evaporation duct profiles. However, the NPS model demonstrated greater stability; specifically, when the EDH is zero or exceeds the boundary layer height, the BYC model may yield zero values for the EDH due to its derivation method, leading to inaccuracies. Consequently, based on existing studies, this article also employs the NPS model to calculate the EDH.

The NPS model utilizes AT, AP, wind speed (WS), relative humidity (RH), and sea surface temperature (SST), which can be collected at the same or different altitudes near the sea surface. Using these inputs, the NPS model generates the modified refractivity profile (M-profile) corresponding to the given environmental conditions. The height corresponding to the minimum refractivity in the M-profile is the EDH. According to the Monin–Obukhov similarity (MOS) theory [43], the vertical profiles of AT and specific humidity (SH) above the near sea surface can be given by:

$$T(z) = T_0 + \frac{\theta_*}{\kappa}\left[\ln\left(\frac{z}{z_{0\theta}}\right) - \Psi_h(\zeta)\right] - \Gamma_d z \tag{5}$$

$$q(z) = q_0 + \frac{q_*}{\kappa}\left[\ln\left(\frac{z}{z_{0\theta}}\right) - \Psi_h(\zeta)\right] \tag{6}$$

where T_0 and q_0 are the AT and SH of the sea surface, respectively; $\zeta = z/L$, L is the Monin–Obukhov length; θ_* and q_* are the related MOS scaling parameters of potential temperature (PT) and SH, respectively; $z_{0\theta}$ and z_{0q} are PT and SH roughness lengths, respectively; Γ_d is dry adiabatic lapse rate; κ is the von Karman constant; and Ψ_h is the temperature correction function. The original NPS model applies the COARE bulk flux algorithm with version 2.6 developed from the Tropical Ocean-Global Atmosphere program for calculating the MOS scaling parameters [44]. To enhance the accuracy and performance of the NPS model, this study applies the upgraded COARE3.0 algorithm to calculate the MOS scaling parameters [45].

Additionally, the original NPS model uses the temperature correction function proposed by Beljaar and Holtslag under stable conditions [46]. However, the Beljjar and Holtslag's correction function has shown suitability exclusively under weak stable conditions, and it tends to yield excessively high EDH in the presence of strong stable conditions [47]. The correction function proposed by Gorbachev et al., derived from the Surface Heat Budget of the Arctic Ocean Experiment (SHEBA), is widely used to calculate turbulent flux [48]. Therefore, the correction function proposed by Gorbachev et al. is used to improve the original correction function and has the following form based on the SHEBA data:

$$\Psi_{h\ SHEBA}(\zeta) = -\frac{b_h}{2}\ln(1 + c_h\zeta + \zeta^2) + \left(-\frac{a_h}{B_h} + \frac{b_h c_h}{2B_h}\right) \times \left(\ln\frac{2\zeta + c_h B_h}{2\zeta + c_h + B_h} - \ln\frac{c_h - B_h}{c_h + B_h}\right) \quad (7)$$

where $a_h \equiv b_h = 5$, $c_h = 3$, and $B_h = \sqrt{c_h^2 - 4} = \sqrt{5}$.

To determine the M-profile near the sea surface, it is essential to obtain the vertical profiles of AP and WVP. The AP profile is determined by integrating the ideal gas law and hydrostatic equation [40] with the following equation:

$$P(z_2) = P(z_1)\exp\left(\frac{g(z_1 - z_2)}{R\overline{T_v}}\right) \quad (8)$$

Furthermore, the WVP profile can be derived from the calculated profiles of SH and AP using the following equation:

$$e(z) = \frac{q(z)P(z)}{\varepsilon + (1 - \varepsilon)q(z)} \quad (9)$$

where $\overline{T_v}$ is the mean value of the virtual temperature at height z_1 and z_2, and ε is a constant with a value of 6.22. According to the AT, SH, and WVP profiles calculated from Equations (5)–(9), the M-profile can be calculated from Equation (4), and thus the EDH can be determined. Based on the given five HMPs, this article uses the NPS model to calculate the M-profile. In the calculated M-profile (see Figure 1), when the modified refractivity is at a minimum value of 353.4 M-units, the corresponding height is EDH, which has a value of 15.7 m [49].

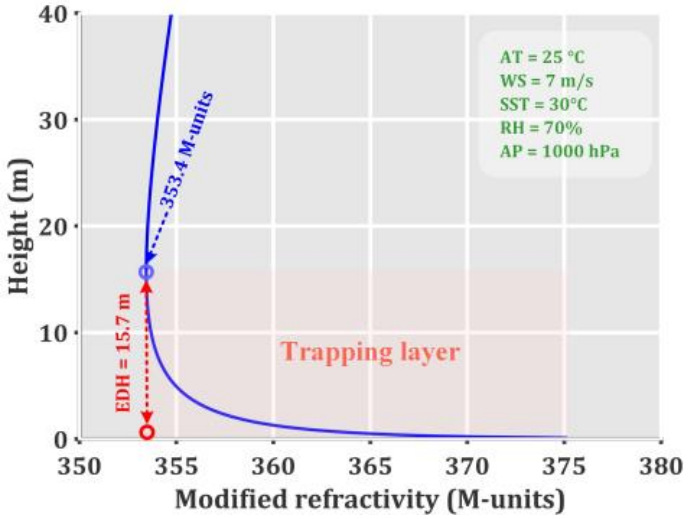

Figure 1. M-profile obtained by the NPS model.

2.4. Calculation of EDH Spatiotemporal Distribution

The study region selected is in the South China Sea (SCS) (4°N–23°N, 105°E–118°E), which is influenced by various tropical circulations and surrounded by many islands and coastlines. These topographies interact with the circulations, resulting in high temperatures and high humidity conditions throughout the year in the SCS.

Firstly, this study extracts the HMPs listed in Table 1 from the ERA5 for the years 2022 and 2023. Figure 2 shows the spatial distribution of AT, AP, and SST, as well as calculated WS and RH, at different time periods in June 2023. Each HMP exhibits regionality and non-uniformity due to varying degrees of meteorological influences across different areas. Consequently, the HMPs within the region demonstrate dynamic characteristics that change over time.

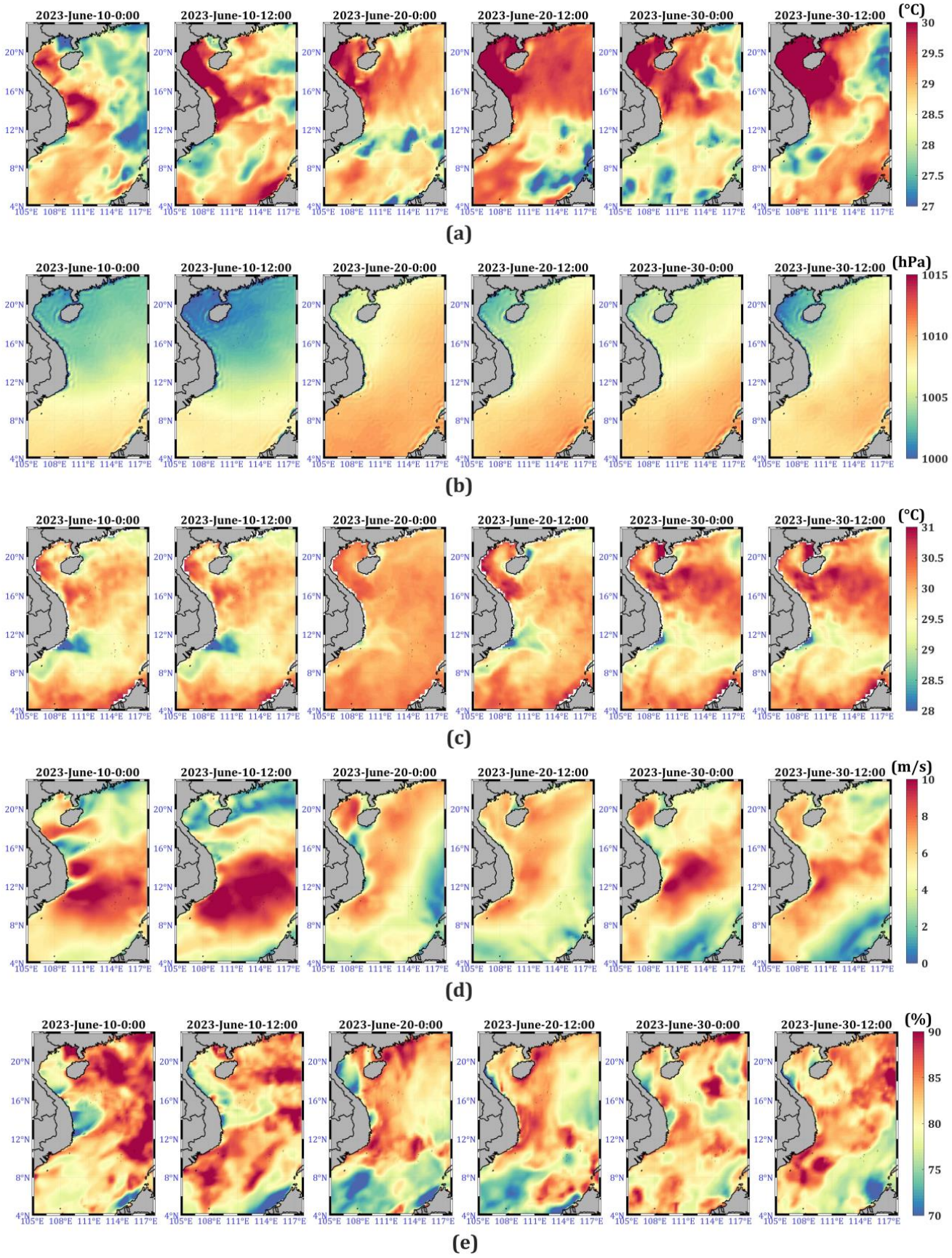

Figure 2. Spatial distributions of (**a**) AT, (**b**) AP, (**c**) SST, (**d**) WS, and (**e**) RH in June 2023.

After calculating the WS and RH, this study inputs them into the NPS model along with AT, AP, and SST to calculate the EDH distribution in the SCS region for the years 2022 and 2023. The ERA5 provides daily reanalysis data with a temporal resolution from 00:00 to 23:00 (UTC). Consequently, each extracted HMP for the two-year period comprises 26,280 spatial distribution samples, while the calculated EDH distribution includes 17,520 samples. The EDH distributions in the SCS during different periods in June are shown in Figure 3. The spatial variations of these HMPs make the evaporation ducts over the large-scale sea surface also regionally non-uniform. Furthermore, as the dynamic characteristics of HMPs vary with time, the evaporation ducts also show temporal dynamic characteristics.

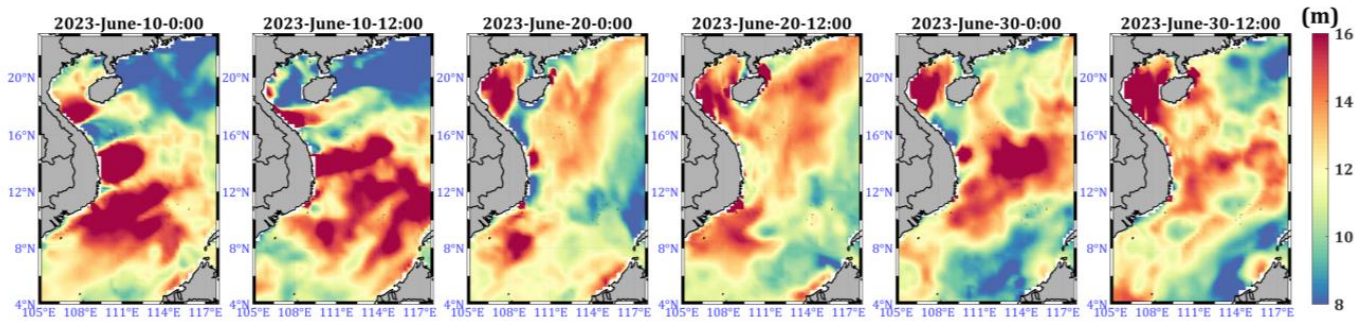

Figure 3. Spatial distributions of calculated EDH in June 2023.

3. Methodology

3.1. Problem Definition

From the perspective of ML, EDH spatial distribution prediction can be viewed as a spatiotemporal sequence prediction problem. This involves the temporal relationships and spatial distributions of EDH grid data. For the EDH distribution in a sea area at moment t, it is represented by a two-dimensional (2D) grid of size $W \times H$. Here, W and H correspond to the number of grids along the longitude and latitude, respectively. Furthermore, the EDH distribution at all moments can be arranged chronologically to form a spatiotemporal sequence of EDH grids [50]. Therefore, a spatiotemporal sequence $\left\{EDH_1, EDH_2, \ldots, EDH_T \middle| EDH_i \in \mathbb{R}^{W \times H}\right\}$ can be obtained, where EDH_i is also a grid of size $W \times H$. The objective of EDH spatiotemporal prediction is to predict the next K distributions in the future given the previous J distributions:

$$EDH_{t+1}^{pred}, EDH_{t+2}^{pred}, \ldots, EDH_{t+K}^{pred} = \mathcal{F}(EDH_{t-J+1}, EDH_{t-J+2}, \ldots, EDH_t) \quad (10)$$

where EDH_i^{pred} is the predicted EDH distribution, and $\mathcal{F}$ is a prediction model. By defining the EDH spatiotemporal prediction, it becomes clear that the EDH spatiotemporal prediction is different from the traditional time sequence prediction. This distinction places higher demands on the prediction model. The model not only needs to accurately capture the temporal characteristics of EDH distributions but also comprehensively account for the spatial correlations among different grid data within the EDH distribution.

3.2. Feature Engineering and HMPs–EDH Mapping Set Construction

To enable the developed prediction model to thoroughly learn the mapping relationships between HMPs and EDH, this article constructs an HMPs–EDH mapping set **(HMP&EDH; EDH)** based on the prediction model's input and output variables, utilizing calculated EDH spatiotemporal sequence and extracted HMPs. Within this mapping set, the model's input **HMP&EDH** is represented as multidimensional feature vectors of HMPs and EDH distributions at different moments. These HMPs include core parameters such as AT, RH, and AP used in EDH calculation, supplemented by additional parameters EVP, SLHF, TP, and SWH. The design of input variables comprehensively considers the multifaceted impact of marine environment for EDH. By incorporating additional HMPs, it

further enhances the mapping relationships between HMPs and EDH. Furthermore, for accurate prediction of EDH, the EDH-STNet model needs to capture the internal temporal relationships within EDH. Therefore, the EDH must also be included as one of the model's input variables, alongside multiple HMPs. Therefore, the model input **HMP&EDH** in the mapping set can be expressed as:

$$\begin{aligned} &\textbf{HMP\&EDH} = \left\{ [HMPs, EDH]_1, \ldots, [HMPs, EDH]_T \middle| [HMPs, EDH]_i \in \mathbb{R}^{10} \right\} \\ &where\ [HMPs, EDH]_i = [AT, RH, WS, AP, SST, EVP, SLHF, TP, SWH, EDH]_i \end{aligned} \tag{11}$$

This article regards the future distribution of EDH as the output of the EDH-STNet model. Therefore, **EDH** is designated as the output variable of the EDH-STNet model and represented by EDH distribution at different moments:

$$\textbf{EDH} = \left\{ EDH_1, EDH_2, \ldots, EDH_T \middle| EDH_i \in \mathbb{R}^1 \right\} \tag{12}$$

3.3. EDH-STNet Model

3.3.1. Principle of the Swin-Unet

Unlike traditional CNNs, the Swin-Unet is the first pure Transformer-based U-shaped architecture [31]. Its basic building module consists of two consecutive Swin-Transformer blocks, where Layer Norm (LN) is applied to standardize the input features, which helps to accelerate the convergence speed and improve training stability. Next, two multi-layer perceptron (MLP) blocks are used to perform nonlinear transformations and feature extraction on the input, in which the Gaussian Error Linear Units activation function can effectively capture the nonlinear relationship in the data. Finally, a window multi-head self-attention (W-MSA) is introduced to capture the long-term dependencies between input features. This windowed design significantly reduces computational complexity while improving the model's scalability and efficiency. The shifted window multi-head self-attention (SW-MSA) function is like W-MSA, but utilizes a sliding window mechanism to calculate attention weights. Self-attention is computed within each window, further decreasing computational complexity and memory consumption. Based on this shifted window mechanism, successive Swin-Transformer blocks can be represented as:

$$\hat{z}^l = \mathrm{W-MSA}(\mathrm{LN}(z^{l-1})) + z^{l-1} \tag{13}$$

$$z^l = \mathrm{MLP}(\mathrm{LN}(\hat{z}^l)) + \hat{z}^l \tag{14}$$

$$\hat{z}^{l+1} = \mathrm{SW-MSA}(\mathrm{LN}(\hat{z}^l)) + \hat{z}^l \tag{15}$$

$$z^{l+1} = \mathrm{MLP}(\mathrm{LN}(\hat{z}^{l+1})) + \hat{z}^{l+1} \tag{16}$$

where $\hat{z}^l$ and z^l are the outputs of the lth W-MSA and MLP, respectively. In the Encoder, a local-to-global self-attention mechanism is implemented, defined by the following self-attention equation:

$$Attention(\mathbf{Q}, \mathbf{K}, \mathbf{V}) = Softmax\left(\frac{\mathbf{Q}\mathbf{K}^\top}{\sqrt{d}} + B\right)\mathbf{V} \tag{17}$$

where $\mathbf{Q} \in \mathbb{R}^{M^2 \times d}$, $\mathbf{K} \in \mathbb{R}^{M^2 \times d}$, and $\mathbf{V} \in \mathbb{R}^{M^2 \times d}$ represent the Query, Key, and Value matrices. M^2 represents the number of patches in the window, and d represents the dimension of the Query or Key. B represents the relative position bias.

3.3.2. Development of the EDH-STNet Model

This article develops a model using Swin-Unet and HMPs specifically to predict the distribution of EDH, as shown schematically in Figure 4. To integrate the Swin-Unet into research on EDH spatiotemporal prediction, several modifications have been made to the network architecture. Firstly, the grid data of EDH and multiple HMPs are concatenated as

inputs, consolidating these variables into a unified 3D matrix. Additionally, linear interpolation and upsampling are performed on this 3D matrix input to ensure consistency in the dimensions of the grid data. Subsequently, the Swin-Transformer blocks in the Encoder extract and abstract features from the input data at multiple levels through their unique W-MSA and SW-MSA mechanisms. These blocks effectively capture spatial information while deepening the understanding of temporal characteristics. Next, the Decoder employs upsampling techniques to progressively reconstruct the advanced features extracted by the Encoder and restore detailed information, thereby generating output that aligns with the original input data. Additionally, in the EDH-STNet model, skip connections are utilized to integrate features from different levels of the Encoder with upsampled features from the Decoder. This design enhances the EDH-STNet model's ability to perceive local information and effectively mitigates spatial information loss caused by downsampling operations. Finally, the advanced features mapped by the EDH-STNet model are outputted through an upsampling layer, which adjusts the spatial resolution of the output features to match the dimensions of the input EDH grid data. Thus, the EDH-STNet model has successfully implemented the ability to predict the distribution of EDH at future moments by integrating multiple HMPs.

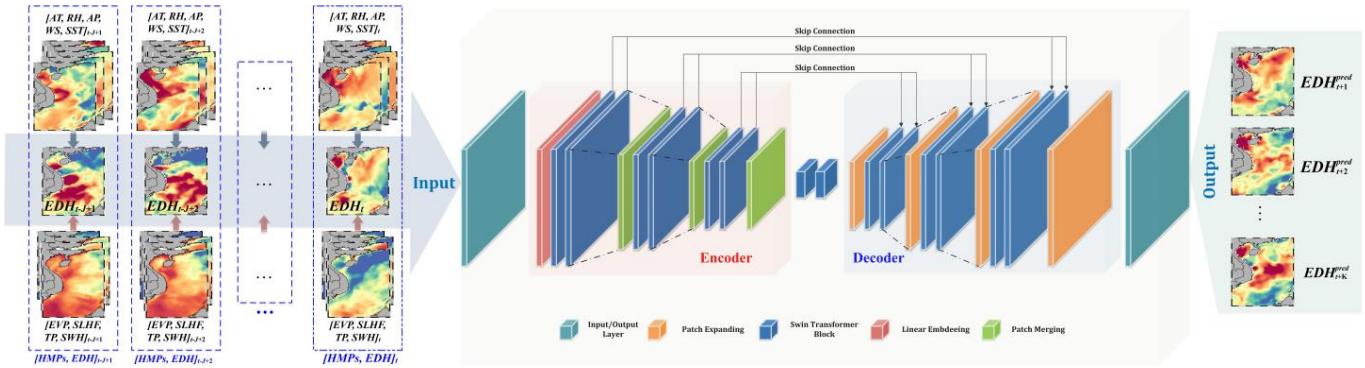

Figure 4. Schematic of the EDH-STNet model.

3.4. Model Training

This article utilizes reanalysis data of meteorological parameters from years 2022 and 2023. To evaluate the EDH-STNet model's performance in predicting EDH spatiotemporal distribution across different years, two HMPs–EDH mapping sets are constructed. Each mapping set is divided into training and test sets in an 80%-to-20% ratio, ensuring the model's generalization capabilities and predictive accuracy during the training process, where the two test sets based on the reanalysis data from years 2022 and 2023 are designated as Test2022 and Test2023, respectively. The two training sets are utilized to train the EDH-STNet model, allowing it to learn the relationships between the input variables and the corresponding output variable through multiple iterative training experiments. The two test sets are used to test the performance of the EDH-STNet model on unseen data. All training experiments in this article were conducted on a Microsoft Windows 10 22H2 system equipped with an Inter Core i7-10700F CPU and an NVIDIA GeForce RTX 4070Ti SUPER 16 GB GPU. Meanwhile, the deep learning programs were developed using Python V3.6.13 and the GPU-based framework PyTorch V1.10.2.

In multiple training experiments, this study comprehensively considers the model efficiency, accuracy, and platform configurations. To achieve optimal training results, hyperparameters such as epochs, batch size, and learning rate are adjusted. Furthermore, to effectively apply the traditional Swin-Unet for predicting EDH distribution, the loss function is modified. The study selects the mean square error (MSE) function, commonly used in regression tasks, as the new loss function. During the model training process, adaptive moment estimation with momentum is employed to optimize the EDH-STNet model for backpropagation [51]. Finally, the configured hyperparameters are as follows—

epochs: 200, batch size: 64, learning rate: 0.001, and momentum: 0.9, with the weight decay 0.0001.

4. Results and Analysis

4.1. Experimental Settings

4.1.1. Evaluation Indicators

To quantitatively evaluate prediction errors and highlight the superiority of the EDH-STNet model, this article calculates the evaluation indicators for all prediction models using the test set. Three categories of indicators are employed, including root mean square error (RMSE), mean absolute error (MAE), and relative RMSE (RRMSE). These indicators are crucial standards for evaluating the performance of prediction models by measuring the mean errors between the predicted results and the test labels. Specifically, smaller values of these indicators indicate relatively lower prediction errors of the model, thereby reflecting a higher accuracy in the model's predictions [52]:

$$\mathrm{RMSE} = \sqrt{\frac{1}{N}\sum_{i=1}^{N}\left(EDH_i - EDH_i^{pred}\right)^2} \tag{18}$$

$$\mathrm{MAE} = \frac{1}{N}\sum_{i=1}^{N}\left|EDH_i - EDH_i^{pred}\right| \tag{19}$$

$$\mathrm{RRMSE} = \left[\mathrm{RMSE}/\left(\frac{1}{N}\sum_{i=1}^{N} EDH_i\right)\right] \tag{20}$$

where N is the size of the test set.

4.1.2. Baseline Models

To demonstrate the advantages of the EDH-STNet model for spatiotemporal prediction of EDH, this article compares it with multiple learning-based methods that serve as baseline models. These baseline models are well-established and validated in existing studies, and are detailed as follows.

1. Unet [53]: In a manner similar to the study in [25], which applies Unet for convective precipitation nowcasting, this study utilizes Unet for EDH spatial distribution prediction and establishes it as a baseline model.
2. *Swin-Transformer* [27]: The Swin-Transformer has been extensively utilized across various fields of CV and has subsequently gained widespread adoption in weather forecasting. Therefore, we employ the Swin-Transformer as a baseline model for the EDH spatiotemporal prediction, comparing it with the EDH-STNet model.
3. *Swin-Unet*: To comprehensively evaluate the impact of HMPs on the prediction performance of the EDH-STNet model, this study establishes an additional EDH spatiotemporal prediction model using Swin-Unet for comparison. A key distinguishing feature of the Swin-Unet model is its exclusion of multiple HMPs from its inputs, focusing solely on EDH spatiotemporal prediction. Additionally, this model was developed using methods consistent with those applied to the EDH-STNet model.
4. *SwinUnet-5*: To verify the enhancement of prediction performance in the EDH-STNet model with the inclusion of additional parameters such as EVP, SLHF, TP, and SWH, this study develops an additional baseline model called SwinUnet-5. This model integrates five HMPs—AT, AP, SST, RH, and WS—and takes EDH as its joint input.

4.2. Prediction Results and Analysis

4.2.1. One-Step Prediction Results and Analysis

First, we input the two test sets into EDH-STNet and the baseline models to obtain their respective prediction results. Subsequently, we visualize the prediction results for both test sets to provide a more intuitive reflection of the models' performance. Furthermore, to evaluate the accuracy of the model predictions, we calculate the absolute error between the

predicted results and the EDH values in the test sets. The partial prediction results from all models for the two test sets are illustrated in Figures 5 and 6, while the partial absolute prediction errors are presented in Figures 7 and 8. The spatial distribution of EDH shows a gradually changing trend over time. This variation is evident not only in the increase or decrease of EDH values but also in the movement of high-EDH regions.

Through a comprehensive analysis of the prediction results and error distributions of all models, we can conclude that the developed EDH-STNet model exhibits superior predictive performance, significantly outperforming the other models. Additionally, the SwinUnet-5 model also demonstrates commendable predictive performance, although it is still inferior to the proposed model. In contrast, the Unet model shows relatively poor predictive performance, indicating its limitations. The main reason for the poor performance of the Unet is the limitation of convolutional operations in the Unet model, which mainly focuses on extracting local spatial correlations and cannot effectively capture temporal characteristics. Meanwhile, the research in [54] indicates that meteorological elements in the marine environment typically do not exhibit significant variations of less than 6 h. This implies a close correlation between the evaporation duct distributions at the previous and subsequent moments. In practice, the neglect of temporal characteristics in the Unet model can cause significant limitations on the EDH spatiotemporal prediction.

The Swin-Transformer outperforms the Unet model. Leveraging its Transformer architecture, Swin-Transformer effectively captures both global and local features. However, despite its excellent performance in feature extraction and representation, the complex structure of the Swin-Transformer introduces gradient propagation issues, thereby limiting its capability to handle long-term dependencies. That is why the predicted EDH of the Swin-Transformer in this article is generally higher than the labels in the test set. This constraint hinders Swin-Transformer from achieving superior predictive performance across extensive spatiotemporal domains. The Swin-Unet, SwinUnet-5, and the EDH-STNet models utilize the Swin-Transformer for construction, which excels in extracting spatial correlations. Moreover, through an Encoder–Decoder structure, all three models effectively capture long-term temporal features in EDH spatiotemporal sequence. Furthermore, the model developed in this article shows higher prediction accuracy. This is primarily attributed to its utilization of a data-driven approach that integrates various marine environmental data as input. This comprehensive input feature design enhances the model's ability to understand complex variations in marine environments, significantly improving the accuracy and reliability of prediction results. The EDH-STNet model leverages the Swin-Transformer block to extract comprehensive spatial correlations of EDH distribution. By effectively capturing temporal characteristics and integrating multiple HMPs, it outperforms all baseline models.

To quantitatively evaluate the prediction errors of all models, this article calculates RMSE, MAE, and RRMSE indicators, as shown in Tables 2 and 3. For Test2022, the Unet exhibits the highest prediction errors, with RMSE, MAE, and RRMSE evaluation indicators of 1.121, 0.708, and 0.214, respectively. It is followed by Swin-Transformer with RMSE, MAE, and RRMSE indicators of 0.968, 0.599, and 0.184, respectively. Compared to the Swin-Transformer model, the Swin-Unet model shows improvements of 14.050%, 18.364%, and 14.130% in its RMSE, MAE, and RRMSE indicators, respectively. This indicates that the Swin-Unet through its unique architectural design can capture dynamic variations and complex patterns in EDH spatiotemporal sequences more effectively compared to the Unet and Swin-Transformer models. Additionally, both the SwinUnet-5 and EDH-STNet models have better indicators than the Swin-Unet model, indicating that the SwinUnet-5 and EDH-STNet models exhibit superior prediction performance. Compared to the Swin-Unet, the SwinUnet-5 model shows improvements of 7.091%, 7.771%, and 6.962% in its three indicators. This indicates that incorporating multiple HMPs as prior information helps the Swin-Unet to more comprehensively understand and capture the complex factors influencing EDH. This improvement not only enhances the Swin-Unet model's accuracy but also increases its interpretability. Additionally, the EDH-STNet model has the best

prediction performance and shows improvements of 12.419%, 6.652%, and 12.245% in its three indicators compared to the SwinUnet-5.

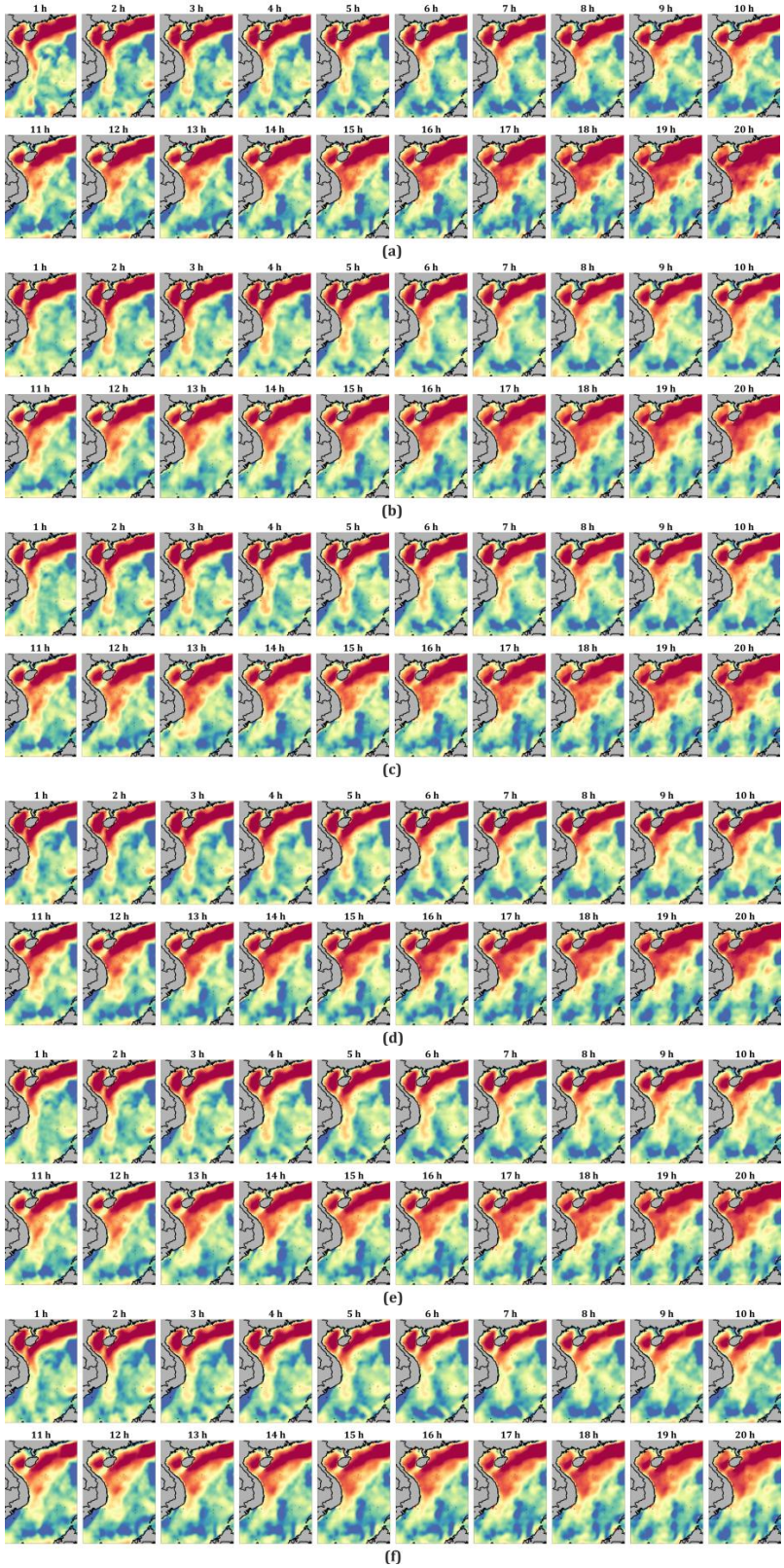

Figure 5. Partial EDH distribution in (**a**) Test2022 and prediction results for the models: (**b**) Unet, (**c**) Swin-Transformer, (**d**) Swin-Unet, (**e**) SwinUnet-5, and (**f**) EDH-STNet.

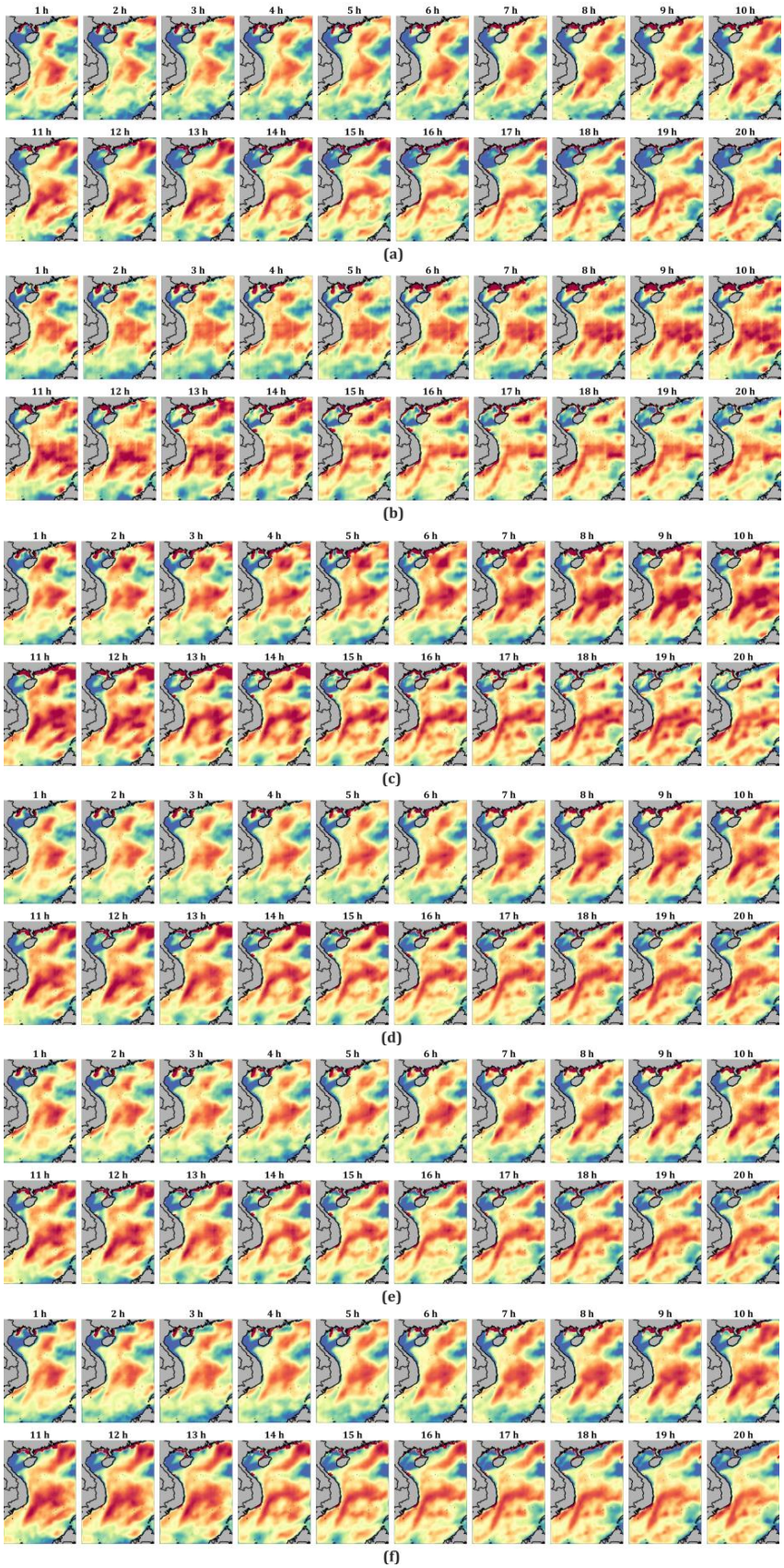

Figure 6. Partial EDH distribution in (**a**) Test2023 and prediction results for the models: (**b**) Unet, (**c**) Swin-Transformer, (**d**) Swin-Unet, (**e**) SwinUnet-5, and (**f**) EDH-STNet.

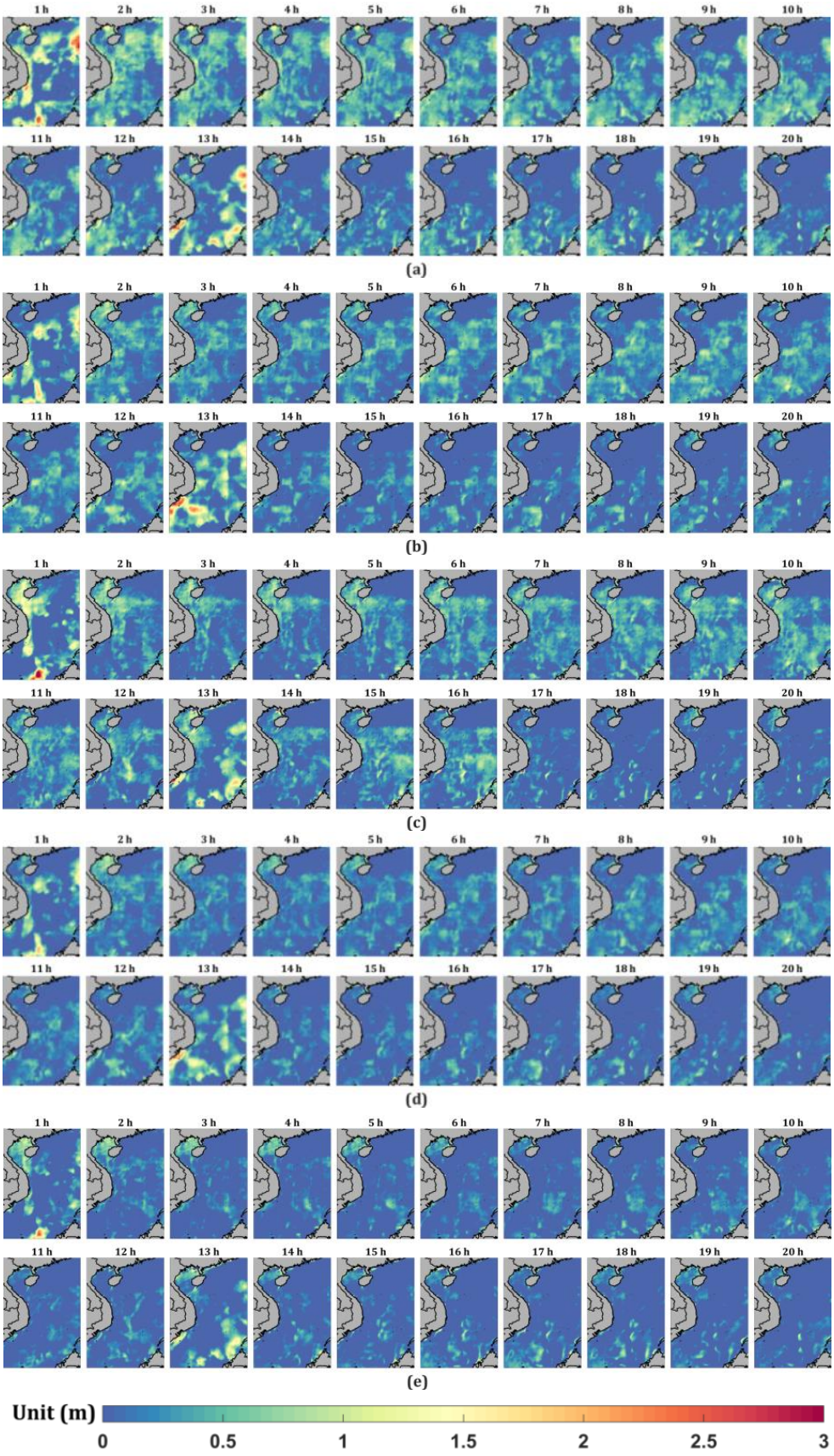

Figure 7. Partial absolute prediction errors of the (**a**) Unet, (**b**) Swin-Transformer, (**c**) Swin-Unet, (**d**) SwinUnet-5, and (**e**) EDH-STNet models on Test2022.

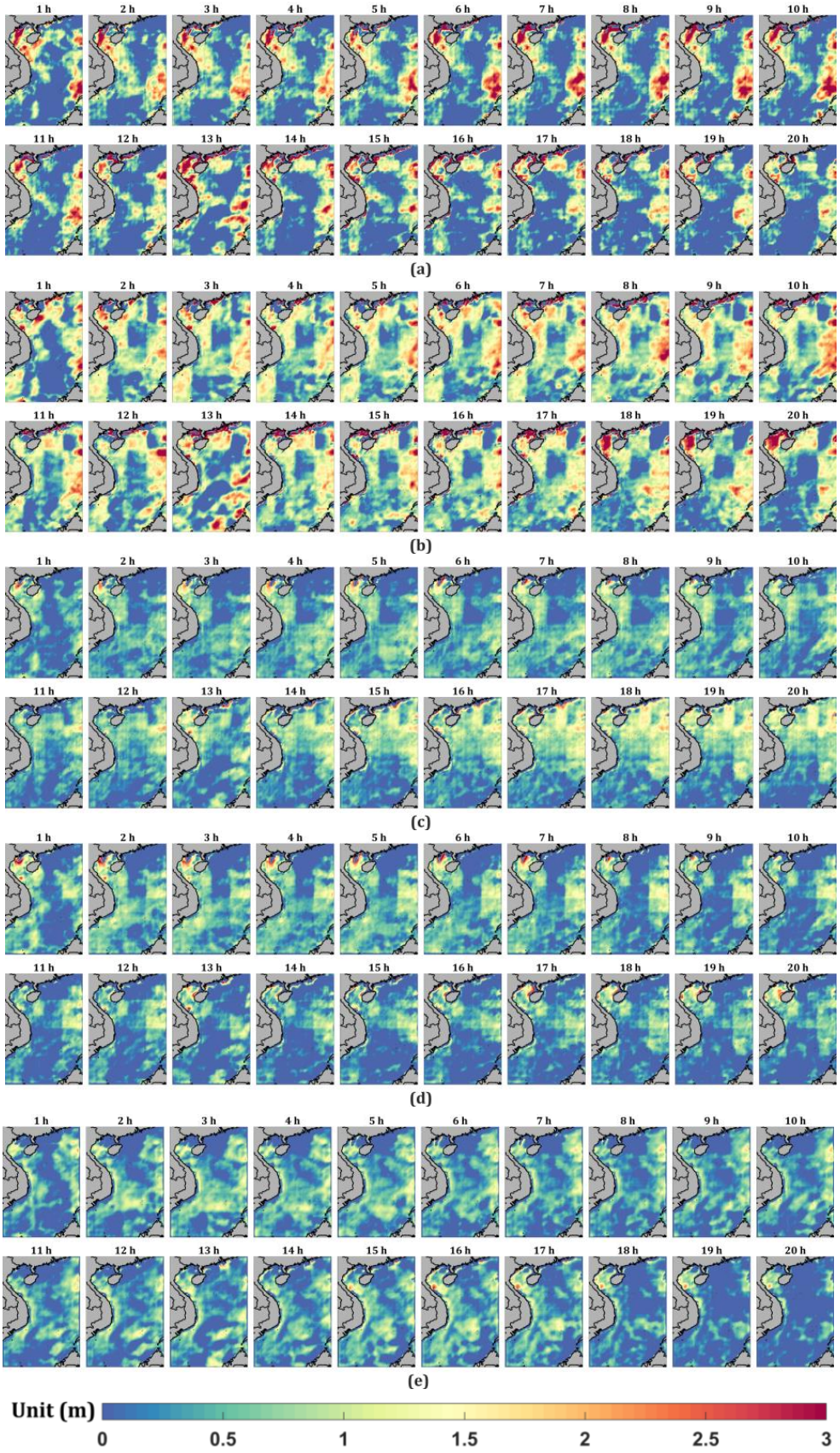

Figure 8. Partial absolute prediction errors of the (**a**) Unet, (**b**) Swin-Transformer, (**c**) Swin-Unet, (**d**) SwinUnet-5, and (**e**) EDH-STNet models on Test2023.

Table 2. Evaluation indicators for Test2022.

Model	Indicator		
	RMSE	**MAE**	**RRMSE**
Unet	1.121	0.708	0.214
Swin-Transformer	0.968	0.599	0.184
Swin-Unet	0.832	0.489	0.158
SwinUnet-5	0.773	0.451	0.147
EDH-STNet	0.677	0.421	0.129

Table 3. Evaluation indicators for Test2023.

Model	Indicator		
	RMSE	**MAE**	**RRMSE**
Unet	1.596	1.014	0.167
Swin-Transformer	1.353	0.839	0.142
Swin-Unet	1.038	0.641	0.109
SwinUnet-5	0.878	0.533	0.092
EDH-STNet	0.793	0.484	0.083

For Test2023, the Unet again demonstrates the highest prediction errors, with RMSE, MAE, and RRMSE evaluation indicators of 1.596, 1.014, and 0.167, respectively. Following this, the Swin-Transformer model has RMSE, MAE, and RRMSE values of 1.353, 0.839, and 0.142, respectively. When compared to the Swin-Transformer model, the Swin-Unet model shows improvements of 23.282%, 23.600%, and 23.239% in its RMSE, MAE, and RRMSE indicators, respectively. Moreover, both the SwinUnet-5 and EDH-STNet models achieve better performance metrics than the Swin-Unet model, indicating their superior prediction capabilities. Specifically, the SwinUnet-5 model improves upon the Swin-Unet by 15.414%, 16.849%, and 15.596% in RMSE, MAE, and RRMSE, respectively. The EDH-STNet model exhibits the best predictive performance overall. This indicates that the additional introduction of HMPs helps to improve the performance of the model. The utilization of more multi-dimensional environmental information for training enables the EDH-STNet model to better adapt to the dynamic variations in the marine environment, thus providing more accurate prediction results.

4.2.2. Multiple-Step Prediction Results and Analysis

To evaluate the performance of the EDH-STNet model in predicting the EDH distribution for multiple future moments, this study further compares the evaluation indicators of the EDH-STNet model with other baseline models at multiple prediction steps (2, 4, 8, and 16). The evaluation indicators for different prediction steps across the two test sets are presented in Tables 4 and 5. As the prediction steps gradually increase, the prediction errors of all the models also increase significantly, which indicates that the prediction performance of the models keeps worsening with the increase of the prediction step. In addition, as the prediction steps increase, the EDH-STNet model consistently has the smallest prediction errors, followed by the SwinUnet-5 model, and finally the Unet model has the worst prediction performance. This shows the superiority of the EDH-STNet model among all prediction models. In addition, the EDH-STNet model also exhibits superior prediction performance at a prediction step size of 16.

For Test2022, when the prediction step is 2, the RMSE, MAE, and RRMSE indicators of the EDH-STNet model are improved by 39.602%, 46.944%, and 39.759%, respectively, compared to the Unet. Compared with the SwinUnet-5 model, the three indicators of the EDH-STNet model are improved by 12.707%, 18.492%, and 12.791%, respectively. Meanwhile, when the prediction step is 16, the EDH-STNet model's RMSE, MAE, and RRMSE indicators are improved by 31.839%, 33.874% and 31.868%, respectively, compared

to the Unet model, and by 12.948%, 14.711%, and 12.921%, respectively, compared to the SwinUnet-5 model. For Test2023, when the prediction step is set to 2, the EDH-STNet model exhibits improvements of 50.444%, 65.081%, and 50.282% in the three indicators, respectively, compared to the Unet model. In comparison to the SwinUnet-5 model, the EDH-STNet model demonstrates enhancements of 16.617%, 32.623%, and 16.190% in these three indicators, respectively. Additionally, at a prediction step of 16, the three indicators of the EDH-STNet model improve by 33.502%, 43.016%, and 33.457%, respectively, when compared to the Unet model, and by 10.955%, 18.347%, and 10.945%, respectively, compared to the SwinUnet-5 model. Comprehensively, these evaluation indicators highlight the superior prediction performance of the EDH-STNet model, which is significantly better than other models.

Table 4. Evaluation indicators for Test2022.

Multiple-Step	Indicator	Model				
		Unet	**Swin-Transformer**	**Swin-Unet**	**SwinUnet-5**	**EDH-STNet**
2	RMSE	1.308	1.084	0.980	0.905	0.790
	MAE	1.080	0.876	0.778	0.703	0.573
	RRMSE	0.249	0.207	0.187	0.172	0.150
4	RMSE	1.569	1.439	1.382	1.254	0.956
	MAE	1.314	1.167	1.121	1.033	0.755
	RRMSE	0.299	0.274	0.263	0.239	0.182
8	RMSE	1.979	1.832	1.781	1.620	1.347
	MAE	1.654	1.523	1.480	1.359	1.088
	RRMSE	0.377	0.349	0.339	0.309	0.257
16	RMSE	2.387	2.170	1.954	1.869	1.627
	MAE	2.034	1.843	1.652	1.577	1.345
	RRMSE	0.455	0.413	0.372	0.356	0.310

Table 5. Evaluation indicators for Test2023.

Multiple-Step	Indicator	Model				
		Unet	**Swin-Transformer**	**Swin-Unet**	**SwinUnet-5**	**EDH-STNet**
2	RMSE	1.691	1.441	1.193	1.005	0.838
	MAE	1.177	0.948	0.756	0.610	0.411
	RRMSE	0.177	0.151	0.125	0.105	0.088
4	RMSE	1.852	1.737	1.535	1.339	1.030
	MAE	1.375	1.133	1.038	0.780	0.575
	RRMSE	0.194	0.182	0.161	0.140	0.108
8	RMSE	2.133	2.070	1.753	1.571	1.328
	MAE	1.665	1.503	1.206	1.015	0.786
	RRMSE	0.223	0.217	0.183	0.164	0.139
16	RMSE	2.567	2.415	2.211	1.917	1.707
	MAE	1.976	1.732	1.526	1.379	1.126
	RRMSE	0.269	0.253	0.231	0.201	0.178

4.2.3. Performance Testing Based on Measured EDH

To validate the predictive performance of the developed EDH-STNet model, we compared the model's predictions with the measured EDH. The measured EDH data were obtained from a radio environment measurement experiment (REME) conducted by the China Research Institute of Radiowave Propagation (CRIRP) in a coastal area of Maoming City, Guangdong Province. The REME primarily relies on an evaporation duct monitoring system (EDMS) installed along the shore. During the REME, the meteorological sensors

within the EDMS automatically measure AT, RH, WS, and AP. Additionally, the infrared SST-measuring instruments automatically record SST parameters. Subsequently, the EDMS performs preprocessing on the measured HMPs data. After preprocessing, these data are input into the NPS model. The model utilizes these five HMP parameters for computation, ultimately yielding the M-profile. The height corresponding to the minimum value of the modified refractivity is determined as the EDH.

Following detailed measurements conducted on a specific day in November 2023, we successfully obtained multiple sets of EDH data. By matching the collection locations with the nearest grid points of the prediction results, we can effectively extract the corresponding predictions for the measurement times, including outputs from both the EDH-STNet model and the baseline models. As shown in Figure 9, a comparison has been made between the predicted results of all models and the measured EDH. Furthermore, we have computed the corresponding evaluation indicators, with the detailed results presented in Table 6. By analyzing the prediction results, we have found that there are significant errors between the model's predictions and the measured EDH compared to the EDH obtained using the reanalysis data. These errors may primarily arise from significant differences between meteorological reanalysis data and the actual measured HMPs. Specifically, meteorological reanalysis data are often based on a fusion of numerical weather prediction models and observational data, which may not fully capture the complexities of the actual environment. In contrast, the measured HMPs provide more direct and accurate information. Therefore, all models may be biased by the quality of the data source when learning the temporal properties of EDH. However, compared to other models, the developed model still demonstrates superior performance. Specifically, this model exhibits a strong fitting trend in its prediction results. Furthermore, it maintains optimal performance across multiple evaluation indicators, further validating its effectiveness and reliability in practical applications.

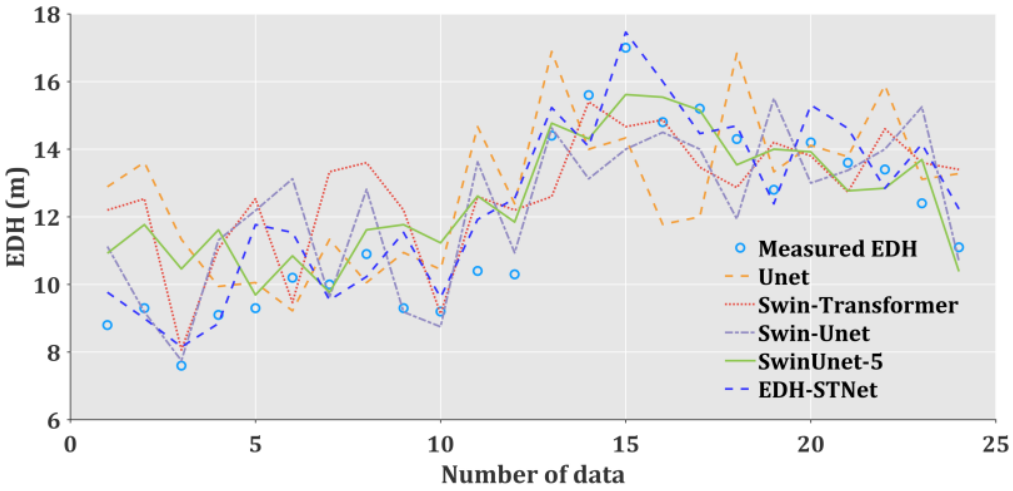

Figure 9. Predictions of all models for measured EDH.

Table 6. Evaluation indicators for the measured EDH.

Model	Indicator		
	RMSE	MAE	RRMSE
Unet	2.365	1.993	0.200
Swin-Transformer	2.012	1.711	0.171
Swin-Unet	1.846	1.453	0.156
SwinUnet-5	1.491	1.237	0.126
EDH-STNet	1.206	1.023	0.102

5. Conclusions

Although machine-learning-based models for predicting EDH have seen significant advancements, challenges remain in accurately predicting EDH distributions across large-scale regions. To address these limitations, we introduce the EDH-STNet model, a novel approach that integrates various environmental information sources and employs the Swin-Unet framework to enhance spatial predictions of EDH. The EDH-STNet utilizes an advanced Encoder–Decoder architecture, with both components consisting of consecutive Swin-Transformer blocks. This design effectively captures complex spatial correlations and temporal dynamics. By incorporating multiple HMPs, the model improves prediction accuracy by capturing the nonlinear relationships between HMPs and EDH. The integration of these additional HMPs allows the EDH-STNet to refine its understanding of the environmental variables influencing EDH, significantly enhancing both the model's accuracy and reliability. This integration occurs through a data-driven methodology, incorporating HMPs as prior information into the EDH-STNet model, which is crucial for refining spatiotemporal predictions. It enables the model to leverage historical and real-time environmental data more effectively. Comprehensive testing and evaluation reveal that the EDH-STNet model, with its sophisticated deep learning algorithms and enriched environmental input, not only delivers precise predictions of EDH for immediate future moments but also offers reliable forecasts for multiple future time frames. The implications of this development are substantial for atmospheric science and radio communications. By providing a robust tool for predicting EDH, the EDH-STNet enhances the stable operation of radio systems, improving their performance under varying atmospheric conditions. This advancement marks a significant step forward in addressing the challenges of large-scale EDH prediction and ensuring the reliability of communication systems reliant on accurate atmospheric modeling.

Author Contributions: Conceptualization, H.J. and L.G.; methodology, H.J. and J.Z.; validation, Y.W.; investigation, Y.W.; resources, X.G.; data curation, Y.Z.; writing—original draft preparation, H.J.; writing—review and editing, Y.W.; visualization, L.G.; supervision, J.Z.; project administration, X.G. and Y.Z.; funding acquisition, L.G. and Y.W. All authors have read and agreed to the published version of the manuscript.

Funding: This work was supported by the National Natural Science Foundation of China (Grant Nos. U21A20457, 62231021, U2006207, 62371380, and 62271457).

Data Availability Statement: The ERA5 reanalysis data can be downloaded through the link (https://cds.climate.copernicus.eu/datasets/reanalysis-era5-single-levels?tab=overview) provided by ECMWF, accessed on 1 January 2022. For the measured evaporation duct data presented in this article, interested parties are welcome to contact us at the email address (jhjxd@stu.xidian.edu.cn), and we will do our best to assist.

Acknowledgments: The authors thank the ECMWF for providing the ERA5 reanalysis data and CRIRP for supplying the measured evaporation duct data.

Conflicts of Interest: The authors declare no conflicts of interest.

References

1. Hitney, H.V.; Richter, J.H.; Pappert, R.A.; Anderson, K.D.; Baumgartner, G.B. Tropospheric radio propagation assessment. *Proc. IEEE* **1985**, *73*, 265–283. [CrossRef]
2. Zhang, J. Methods of Retrieving Tropospheric Ducts Above Ocean Surface Using Radar Sea Clutter and GPS Signals. Ph.D. Thesis, Xidian University, Xi'an, China, 2012.
3. Ji, H.; Guo, L.; Zhang, J.; Wei, Y.; Guo, X.; Zhang, Y.; Nie, T.; Feng, J. IPILT–OHPL: An Over-the-Horizon Propagation Loss Prediction Model Established by Incorporating Prior Information Into the LSTM–Transformer Structure. *IEEE J. Sel. Top. Appl. Earth Observ. Remote Sens.* **2024**, *17*, 10067–10082. [CrossRef]
4. Gilles, M.A.; Earls, C.; Bindel, D. A Subspace Pursuit Method to Infer Refractivity in the Marine Atmospheric Boundary Layer. *IEEE Trans. Geosci. Remote Sens.* **2019**, *57*, 5606–5617. [CrossRef]
5. Fountoulakis, V.; Earls, C. Inverting for Maritime Environments Using Proper Orthogonal Bases from Sparsely Sampled Electromagnetic Propagation Data. *IEEE Trans. Geosci. Remote Sens.* **2016**, *54*, 7166–7176. [CrossRef]

6. Isaakidis, S.A.; Dimou, I.N.; Xenos, T.D.; Dris, N.A. An artificial neural network predictor for tropospheric surface duct phenomena. *Nonlinear Process Geophys.* **2007**, *14*, 569–573. [CrossRef]
7. Yan, X.; Yang, K.; Ma, Y. Calculation Method for Evaporation Duct Profiles Based on Artificial Neural Network. *IEEE Antennas Wirel. Propag. Lett.* **2018**, *17*, 2274–2278. [CrossRef]
8. Zhu, X.; Li, J.; Zhu, M.; Jiang, Z.; Li, Y. An Evaporation Duct Height Prediction Method Based on Deep Learning. *IEEE Geosci. Remote Sens. Lett.* **2018**, *15*, 1307–1311. [CrossRef]
9. Zhao, W.; Li, J.; Zhao, J.; Zhao, D.; Zhu, X. PDD_GBR: Research on Evaporation Duct Height Prediction Based on Gradient Boosting Regression Algorithm. *Radio Sci.* **2019**, *54*, 949–962. [CrossRef]
10. Zhao, W.P.; Li, J.; Zhao, J.; Zhao, D.; Lu, J.; Wang, X. XGB Model: Research on Evaporation Duct Height Prediction Based on XGBoost Algorithm. *Radioengineering* **2020**, *29*, 81–93. [CrossRef]
11. Zhao, W.; Li, J.; Zhao, J.; Jiang, T.; Zhu, J.; Zhao, D.; Zhao, J. Research on evaporation duct height prediction based on back propagation neural network. *IET Microw. Antennas Propag.* **2020**, *14*, 1547–1554. [CrossRef]
12. Mai, Y.; Sheng, Z.; Shi, H.; Li, C.; Liu, L.; Liao, Q.; Zhang, W.; Zhou, S. A New Diagnostic Model and Improved Prediction Algorithm for the Heights of Evaporation Ducts. *Front. Earth Sci.* **2020**, *8*, 102. [CrossRef]
13. Mai, Y.; Sheng, Z.; Shi, H.; Li, C.; Liao, Q.; Bao, J. A New Short-Term Prediction Method for Estimation of the Evaporation Duct Height. *IEEE Access.* **2020**, *8*, 136036–136045. [CrossRef]
14. Han, J.; Wu, J.; Zhu, Q.; Wang, H.; Zhou, Y.; Jiang, M.; Zhang, S.; Wang, B. Evaporation Duct Height Nowcasting in China's Yellow Sea Based on Deep Learning. *Remote Sens.* **2021**, *13*, 1577. [CrossRef]
15. Hong, F.; Zhang, Q. Time Series Analysis of Evaporation Duct Height over South China Sea: A Stochastic Modeling Approach. *Atmosphere* **2021**, *12*, 1663. [CrossRef]
16. Zhao, W.; Zhao, J.; Li, J.; Zhao, D.; Huang, L.; Zhu, J.; Lu, J.; Wang, X. An Evaporation Duct Height Prediction Model Based on a Long Short-Term Memory Neural Network. *IEEE Trans. Antennas Propag.* **2021**, *69*, 7795–7804. [CrossRef]
17. Liao, Q.; Mai, Y.; Sheng, Z.; Wang, Y.; Ni, Q.; Zhou, S. The Comparison of Long Short-Term Memory Neural Network and Deep Forest for the Evaporation Duct Height Prediction. *IEEE Trans. Antennas Propag.* **2023**, *71*, 4444–4450. [CrossRef]
18. Chai, X.; Li, J.; Zhao, J.; Wang, W.; Zhao, X. LGB-PHY: An Evaporation Duct Height Prediction Model Based on Physically Constrained LightGBM Algorithm. *Remote Sens.* **2022**, *14*, 3448. [CrossRef]
19. Cheng, Y.; Xu, J.; Zhang, Y.; Guo, X.; You, Z. Influence of sea surface temperature on numerical simulation of lower atmospheric duct over the South China Sea. *Chin. J. Radio Sci.* **2022**, *37*, 40–47. (In Chinese)
20. Cheng, Y.; Zha, M.; You, Z.; Zhang, Y. Duct climatology over the South China Sea based on European Center for Medium Range Weather Forecast reanalysis data. *J. Atmos. Sol. Terr. Phys.* **2021**, *222*, 105720. [CrossRef]
21. Zhang, P.; Zhang, S.; Zhang, L.; Guo, X.; Han, J. Comparison between predicted and experimental result of regional evaporation duct over sea. *Chin. J. Radio Sci.* **2017**, *32*, 215–220. (In Chinese)
22. ITU-R Recommendation P.453-14. *The Radio Refractive Index: Its Formula and Refractivity Data*; ITU: Geneva, Switerland, 2012.
23. Hao, X.; Li, Q.; Guo, L.; Lin, L.; Ding, Z.; Zhao, Z.; Yi, W. Digital maps of atmospheric refractivity and atmospheric ducts based on a meteorological observation datasets. *IEEE Trans. Antennas Propag.* **2022**, *70*, 2873–2883. [CrossRef]
24. Heidler, K.; Mou, L.; Baumhoer, C.; Dietz, A.; Zhu, X.X. HED-UNet: Combined Segmentation and Edge Detection for Monitoring the Antarctic Coastline. *IEEE Trans. Geosci. Remote Sens.* **2022**, *60*, 4300514. [CrossRef]
25. Han, L.; Liang, H.; Chen, H.; Zhang, W.; Ge, Y. Convective Precipitation Nowcasting Using U-Net Model. *IEEE Trans. Geosci. Remote Sens.* **2022**, *60*, 4103508. [CrossRef]
26. Dosovitskiy, A.; Beyer, L.; Kolesnikov, A.; Weissenborn, D.; Zhai, X.; Unterthiner, T.; Dehghani, M.; Minderer, M.; Heigold, G.; Gelly, S.; et al. An image is worth 16×16 words: Transformers for image recognition at scale. *arXiv* **2010**, arXiv:11929.2020.
27. Liu, Z.; Lin, Y.; Cao, Y.; Hu, H.; Wei, Y.; Zhang, Z.; Lin, S.; Guo, B. Swin Transformer: Hierarchical Vision Transformer using Shifted Windows. In Proceedings of the 2021 IEEE/CVF International Conference on Computer Vision (ICCV), Montreal, QC, Canada, 11–17 October 2021.
28. Bojesomo, A.; Al-Marzouqi, H.; Liatsis, P. Spatiotemporal Vision Transformer for Short Time Weather Forecasting. In Proceedings of the 2021 IEEE International Conference on Big Data (Big Data), Orlando, FL, USA, 15–18 December 2021.
29. Bojesomo, A.; AlMarzouqi, H.; Liatsis, P. A Novel Transformer Network with Shifted Window Cross-Attention for Spatiotemporal Weather Forecasting. *IEEE J. Sel. Top. Appl. Earth Observ. Remote Sens.* **2024**, *17*, 45–55. [CrossRef]
30. Kavitha, S.; Nagamani, H.S.; Sumanth, S.; Pareek, P.K.; Mageswari, P.U. Weather Forecasting Using Advanced Artificial Intelligence Techniques Based on Swin Transformer Network. In Proceedings of the 2024 International Conference on Distributed Computing and Optimization Techniques (ICDCOT), Bengaluru, India, 15–16 March 2024; pp. 1–6.
31. Cao, H.; Wang, Y.; Chen, J.; Jiang, D.; Zhang, X.; Tian, Q.; Wang, M. Swin-unet: Unet-like pure transformer for medical image segmentation. *arXiv* **2021**, arXiv:2105.05537.
32. Huang, L.; Zhao, X.; Liu, Y.; Yang, P.; Ding, J.; Zhou, Z. The Diurnal Variation of the Evaporation Duct Height and Its Relationship with Environmental Variables in the South China Sea. *IEEE Trans. Antennas Propag.* **2022**, *70*, 10865–10875. [CrossRef]
33. Alduchov, O.A.; Eskridge, R.E. Improved Magnus Form Approximation of Saturation Vapor Pressure. *J. Appl. Meteorol.* **1996**, *35*, 601–609. [CrossRef]
34. Lawrence, M.G. The Relationship between Relative Humidity and the Dewpoint Temperature in Moist Air: A Simple Conversion and Applications. *Bull. Amer. Meteorol. Soc.* **2005**, *86*, 225–233. [CrossRef]

35. Wang, S.; Yang, K.; Shi, Y.; Yang, F.; Zhang, H.; Ma, Y. Prediction of Over-the-Horizon Electromagnetic Wave Propagation in Evaporation Ducts Based on the Gated Recurrent Unit Network Model. *IEEE Trans. Antennas Propag.* **2023**, *71*, 3485–3496. [CrossRef]
36. Zhang, Q.; Yang, K.; Yang, Q. Statistical Analysis of the Quantified Relationship between Evaporation Duct and Oceanic Evaporation for Unstable Conditions. *J. Atmos. Ocean. Technol.* **2017**, *34*, 2489–2497. [CrossRef]
37. Benhmammouch, O.; Caouren, N.; Khenchaf, A. Modeling of roughness effects on electromagnetic waves propagation above sea surface using 3D parabolic equation. In Proceedings of the 2009 IEEE International Geoscience and Remote Sensing Symposium, Cape Town, South Africa, 12–17 July 2009; pp. 817–820.
38. Skolnik, M.I. *Introduction to Radar Systems*; McGraw-Hill: New York, NY, USA, 1962.
39. Aires, F.; Prigent, C.; Orlandi, E.; Milz, M.; Eriksson, P.; Crewell, S.; Lin, C.; Kangas, V. Microwave hyperspectral measurements for temperature and humidity atmospheric profiling from satellite: The clear-sky case. *J. Geophys. Res.* **2015**, *120*, 311–334. [CrossRef]
40. Babin, S.M.; Dockery, G.D. LKB-Based Evaporation Duct Model Comparison with Buoy Data. *J. Appl. Meteorol.* **2002**, *41*, 434–446. [CrossRef]
41. Paulus, R.A. Practical application of an evaporation duct model. *Radio Sci.* **1985**, *20*, 887–896. [CrossRef]
42. Babin, S.M.; Young, G.S.; Carton, J.A. A New Model of the Oceanic Evaporation Duct. *J. Appl. Meteorol.* **1997**, *36*, 193–204. [CrossRef]
43. Foken, T. 50 years of the Monin-Obukhov similarity theory. *Bound. Layer Meteor.* **2006**, *119*, 431–447. [CrossRef]
44. Fairall, C.W.; Bradley, E.F.; Rogers, D.P.; Edson, J.B.; Young, G.S. Bulk parameterization of air-sea fluxes for Tropical Ocean-Global Atmosphere Coupled-Ocean Atmosphere Response Experiment. *J. Geophys. Res.* **1996**, *101*, 3747–3764. [CrossRef]
45. Fairall, C.W.; Bradley, E.F.; Hare, J.E.; Grachev, A.A.; Edson, J.B. Bulk Parameterization of Air-Sea Fluxes: Updates and Verification for the COARE Algorithm. *J. Clim.* **2003**, *16*, 571–591. [CrossRef]
46. Beljaars, A.C.M.; Holtslag, A.A.M. Flux Parameterization over Land Surfaces for Atmospheric Models. *J. Appl. Meteorol.* **1991**, *30*, 327–341. [CrossRef]
47. Shi, Y.; Yang, K.; Yang, Y.; Ma, Y. A New Evaporation Duct Climatology over the South China Sea. *J. Meteorol. Res.* **2015**, *29*, 764–778. [CrossRef]
48. Grachev, A.A.; Andreas, E.L.; Fairall, C.W.; Guest, P.S.; Persson, P.O.G. SHEBA flux-profile relationships in the stable atmospheric boundary layer. *Bound. Layer Meteor.* **2007**, *124*, 315–333. [CrossRef]
49. Zhang, J.; Wu, Z.; Zhu, Q.; Wang, B. A Four-Parameter M-Profile Model for the Evaporation Duct Estimation from Radar Clutter. *Prog. Electromagn. Res.* **2011**, *114*, 353–368. [CrossRef]
50. Shi, X.; Chen, Z.; Wang, H.; Yeung, D.-Y.; Wong, W.; Woo, W. Convolutional LSTM Network: A Machine Learning Approach for Precipitation Nowcasting. *Adv. Neural Inf. Process. Syst.* **2015**, *28*, 802–810.
51. Kingma, D.P.; Ba, J. Adam: A Method for Stochastic Optimization. *arXiv* **2015**, arXiv:1412.6980.
52. Ye, M.; Li, B.; Nie, J.; Qian, Y.; Yang, L. Ca-STANet: Spatiotemporal Attention Network for Chlorophyll-a Prediction with Gap-Filled Remote Sensing Data. *IEEE Trans. Geosci. Remote Sens.* **2023**, *61*, 4203314. [CrossRef]
53. Ronneberger, O.; Fischer, P.; Brox, T. U-Net: Convolutional Networks for Biomedical Image Segmentation. *arXiv* **2015**, arXiv:1505.04597.
54. Rasp, S.; Dueben, P.D.; Scher, S.; Weyn, J.A.; Mouatadid, S.; Thuerey, N. WeatherBench: A Benchmark Data Set for Data-Driven Weather Forecasting. *J. Adv. Model. Earth Syst.* **2020**, *12*, e2020MS002203. [CrossRef]